

MAPS (Martian Pit Shadow Extractor)

Abstract

Pits, or collapse pits, are circular-to-elliptical depressions in planetary surfaces that do not exhibit a raised rim. They are generally formed by gravitational collapse into an underground void, or by the evacuation or removal of subsurface material. For this, pits are highly interesting geological features. However, they could also be crucial for future space exploration, as they provide shelter from harmful radiation and could even be a source of ice water on Mars. Previous work has provided a method of calculating the apparent depth (h) of Martian pits by manually measuring the width of its shadow in remote-sensing imagery [1]. h is known as the depth at the edge of the shadow within the pit interior. However, having an automated method would allow the calculation of h for far larger datasets of Martian pits, which could be used for further research or engineering use.

This report describes the purpose, methodology, and testing results of the Martian Pit Shadow extractor (MAPS) tool. MAPS is an automated Python framework which employs K-Means clustering to extract the shadow from a cropped red-band Mars Reconnaissance Orbiter HiRISE image of a Martian pit. MAPS also uses the sensing information from each image in order to determine h using the method from Wyrick et al. [1]. MAPS is designed to be used as a post-processing tool after Martian pits have been automatically detected, perhaps through the use of machine learning. While MAPS is currently specific only to the HiRISE sensor, the method described in this report is highly applicable to other sensors and other planetary data.

MAPS was initially tested on three features from the Mars Global Cave Candidate Catalog (MGC³) which were covered by the HiRISE-derived digital terrain model. This confirmed that the MAPS tool was predicting h values on the correct order of magnitude, and also raised concerns that changes in the emission angle of the HiRISE camera may cause significant variation for h between images of the same feature. As a result, 123 HiRISE images were retrieved for 88 appropriate MGC³ atypical pit craters (APCs) and passed through the MAPS tool, in order to further investigate. The main results from this stage of testing showed that there is no correlation between the size of the pit and the relative uncertainty in h as found by MAPS, and that large changes in emission angles were in fact the cause of h variation between images of the same APC.

There is scope for future work in calibrating the parameters of the MAPS tool, such as the values of k used for K-Means clustering and the maximum emission angle allowed for an image, in order to improve the confidence in the outputted shadow shapefile and h values. This may be possible by testing artificially created elevation data and images of pits, or by considering the morphology of surrounding surface pixels as a means of making shadow detections more concrete.

Contents

1	Introduction	3
1.1	Pits in the Solar System	3
1.2	Previous Work	3
1.3	MAPS: Martian Pit Shadow Extractor	4
2	Methodology	4
2.1	Shadow Extraction Using K-Means Clustering	4
2.2	Apparent Depth Calculation	7
2.3	Error Analysis	8
2.4	Initial Testing for Comparison with Elevation Data	9
2.5	Testing on 88 Atypical Pit Craters	11
3	Results and Discussion	12
3.1	Results of Initial Testing	12
3.2	Results of Testing on 88 Atypical Pit Craters	13
4	Limitations and Future Improvement	17
5	Conclusion	18
6	Appendix	20

1 Introduction

1.1 Pits in the Solar System

Pits are types of planetary surface features which exhibit a circular-to-elliptical depression with no raised rim. It is this lack of a raised extent, or ejecta blanket, that is the main distinguishing factor between a pit and an impact crater. Due to the several hypothesised formation mechanisms which can form features that fit this description, there exists many sub-types of pits. According to the Encyclopedia of Planetary Landforms [2], these sub-types largely fall into two main categories: those which are formed via volcanism or faulting; and those which are not.

Pits which are formed by volcanic processes [3], or by faulting in the surface [4], are intended to be known as ‘pit craters’. Interestingly, should the size of a pit crater exceed 1 km in diameter for Earth, or roughly 10 km for other planetary bodies, they are instead known as calderas [5, 6]. Pit craters are commonly found within the Solar System to be aligned into chains [7], which can lead to further collapses forming linear and sinuous troughs [8, 1]. One suggestion for how this alignment occurs is due to the evacuation of lava tubes [1]. Lava tubes are sinuous conduits of past or presently flowing lava underneath the surface [9]. Lava tubes on other planetary bodies are estimated to be significantly larger than their Earth analogues due to the lower gravitational attraction [10]. These features are of particular interest for future robotic and crewed space exploration as they can provide shelter from harmful radiation, and could also be a source of ice water on Mars [11].

It is also possible for pits to emerge without volcanic or seismic activity. For example, pits have been observed in impact melt deposits on the Moon, most probably caused by collapse into a sub-surface cavity formed via the draining of sub-surface molten melt [2, 12]. Degassing of volatiles from the centres of impact craters, as well as sublimation of sub-surface ices, can also produce depressions that are classed as pits [2].

Attempts have been made to use automated techniques, such as deep learning [13, 14], to detect pits in remote-sensing imagery. This is crucial for building larger, more global databases of pits on Solar System bodies, since many manual surveys have only focused on specific regions (such as the Tharsis region on Mars [15]). With a global dataset, and a suitable tool for estimating pit depths from visual imagery, the deepest pits could be identified for future robotic exploration and potential habitation for crewed missions. If a similar tool could also extract the shadows cast by the Sun onto the interior of pits, then this could be used as pseudo-labels for training deep learning models for detecting pits. The term ‘pseudo-labels’ is deliberately used here in place of calling them ground truth as the shadow would not have been manually labelled.

1.2 Previous Work

Previous work has studied the distribution and morphology of pit crater chains on the surface of Mars [1]. Within this survey, a method was provided for estimating the true depths and volumes of Martian pits based on the size of their shadows. Assuming that the angle at which the Sun is inclined to the surface is constant, the shadow will cast further across the floor of the pit the deeper the pit is. This study by Wyrick et al. assumes that the interiors of the pits are all conical in volume, as shown in figure 1. Figure 1 has been adapted from figure 3(a) of [1] so that the properties are given consistent notation in this report.

For each pit, the shadow width (x_{sh}) and diameter (D) was measured by Wyrick et al. in ArcViewTM GIS [1]. x_{sh} is defined as the distance along the Sun’s line of sight between the rim of the pit and the edge of the shadow projected into the pit, and D is the distance from rim-to-rim along the same axis. With this information, the apparent depth (h) at the edge of the shadow could be found using equation (1). α is known as the solar incidence angle, which is the angle between the

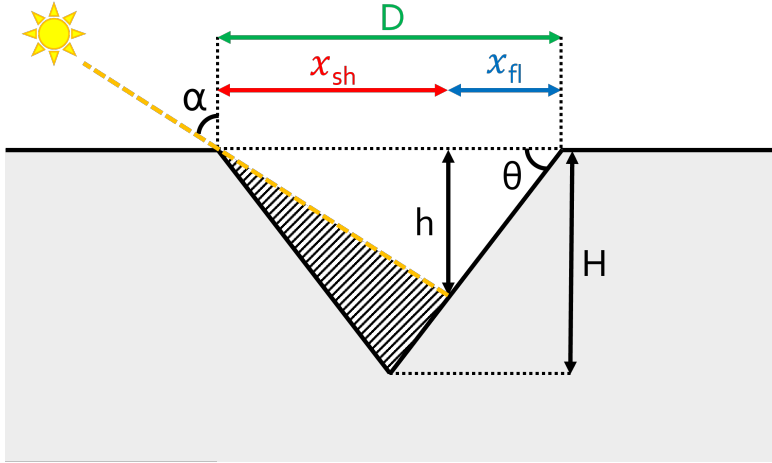


Figure 1: Schematic of how properties of a Martian pit are defined in [1]. This figure is a cross-section of a pit taken along the Sun’s line of sight and has been adapted from figure 3 (a) of [1], so that the properties are given consistent notation in this report. The hashed region represents the section of the pit which is covered in shadow.

Sun and the normal to the surface.

$$\tan(90^\circ - \alpha) = \frac{h}{x_{sh}} \rightarrow h = x_{sh} \tan(90^\circ - \alpha) \quad (1)$$

Since Wyrick et al. assume that all pits are conical, the apparent depth was used to find the slope angle, θ . As the diameters had been measured manually, using equations (2) and (3) allowed for the true pit depth (H) to be calculated.

$$\theta = \arctan\left(\frac{h}{D - x_{sh}}\right) = \arctan\left(\frac{h}{x_{fl}}\right) \quad (2)$$

$$H = \left(\frac{D}{2}\right) \tan \theta \quad (3)$$

Now that H had been calculated, the formula for the volume of a circular cone, $V = (H/3)\pi(D/2)^2$, was applied. However, the authors of the study themselves admit that since not all pits will have a perfectly conical interior, that this volume will often be an upper-bound [1].

1.3 MAPS: Martian Pit Shadow Extractor

The scope of this report is to introduce the Martian Pit Shadow extractor (MAPS) tool, detail its methodology, and discuss the results when applied to some example pits. The purpose of MAPS is to automatically extract the shadow from Martian pits (if one is present) for future analysis, as well as to calculate their apparent depths. The current iteration of MAPS is specific to Mars as it can only read in the metadata labels for Mars Reconnaissance Orbiter (MRO) High Resolution Imaging Science Experiment (HiRISE) Reduced Data Record Version 1.1 (RDRV11) images. The intention is for MAPS to be used as a post-processing tool after some automatic detection has been performed for Martian pits. This is because MAPS can only extract a shadow from an image which is cropped to, and only includes, a pit. Section 2 will explain the approach taken to extract the shadows from Martian pits, and how the apparent depth calculation is conducted.

2 Methodology

2.1 Shadow Extraction Using K-Means Clustering

The MAPS tool was also designed to use equation (1) to calculate the apparent depths of Martian pits, similarly to Wyrick et al. However, as the aim of MAPS is to automate this process, measuring

the shadow width (x_{sh}) using GIS software was not possible and another method was necessary. This problem became two-fold: the first is how to extract the whole shadow from an image of a Martian pit; and the second is how (and where) to measure the width of the extracted shadow.

With regards to the former, previous attempts at automating shadow extraction from Martian pits took the entire range of pixel values and classified the lowest octile as the shadow [13]. This is likely an appropriate assumption for the most regularly-shaped pits. Although if an image of a pit has a greater range of pixel values when compared to another, then the threshold for what is classified as a shadow pixel has changed. Even normalising the images to a consistent bounds of pixel values (for example from 0 to 255) would not solve this as the range of present pixel values still remains, just on a new scale. This means that there is the risk that many non-shadow pixels could be classified as a shadow, just because they are relatively dark compared to the brightest pixels.

It was for this reason that K-Means clustering was chosen as the method for separating the shadow from the remainder of the image. K-Means is a popular unsupervised machine learning algorithm which aims to cluster n data points (in this case n pixels) into k number of clusters. As it is a Python framework, MAPS uses the scikit learn K-Means clustering function (see <https://scikit-learn.org/stable/modules/clustering.html#k-means> for more details). The output of applying this function is an array (of the same size as the input image) containing values which indicate which cluster the pixel belongs to. The clusters are arbitrarily assigned an integer value from 0 to $k - 1$, which became a problem when attempting to select which cluster(s) contains a shadow. As such, the average pixel value from the input image for each cluster is calculated and then the clusters are re-assigned values from 0 to $k - 1$ according to how dark they are (with 0 being darkest). An example of these sorted clusters is displayed in figure 2.

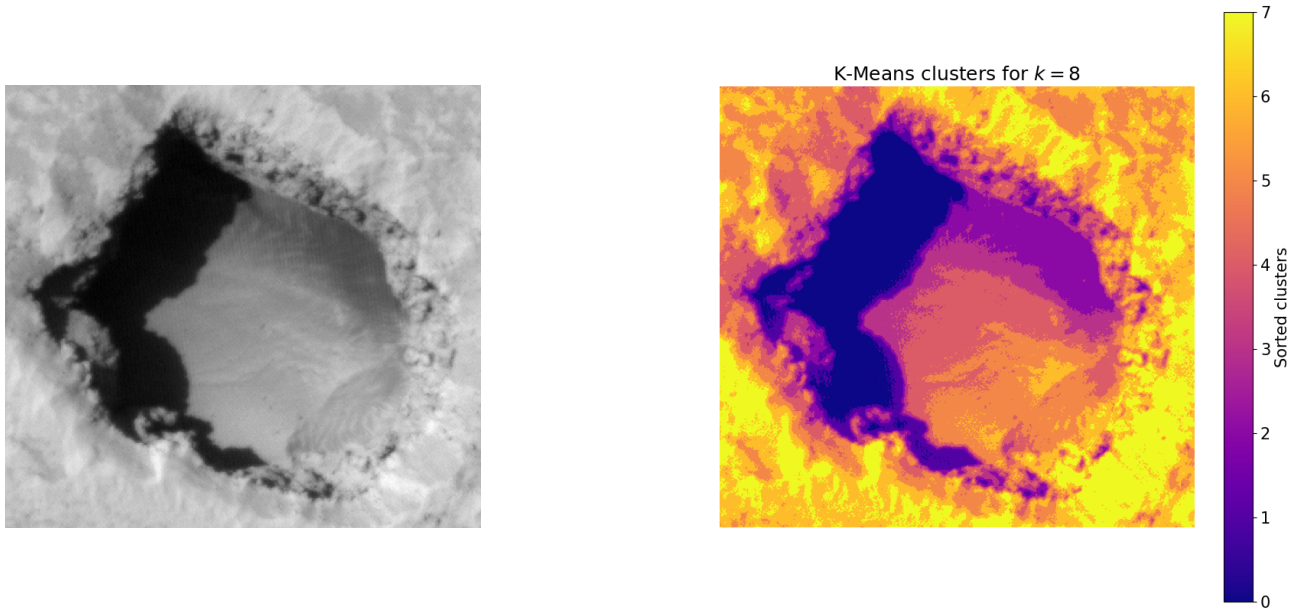


Figure 2: Result of performing K-Means clustering (into eight clusters) on an image of the MGC³ feature APC130. (Left) The input red-band image of APC130, ESP_052638_2020. (Right) ESP_052638_2020 segmented into eight separate clusters thanks to the K-Means algorithm. While $k = 8$ in this case, MAPS iterates over several values of k . Assigned cluster values are sorted by the average pixel values from the input that the cluster covers, with 0 being the darkest cluster.

From this array of sorted clusters, if a cluster was found to have an average value of less than 30, then it was classified as a shadow. This shadow cluster was then converted into a binary mask where the pixel is assigned a 1 if it is a shadow and 0 where it is not. In the event that multiple clusters are sufficiently dark, they are all merged into this binary shadow mask. 30 was chosen as the pixel value threshold as it was found to reliably extract the shadow cluster, without including those which are visibly too bright, during testing on some examples.

However, in the early development of the MAPS tool, it was noticed that the number of clusters (n) that was chosen led to differently-sized shadow masks being produced. This meant that the factor that would contribute the most uncertainty when measuring the shadow width was the number of clusters, rather than the resolution of the image when counting pixels. In order to quantify this, MAPS takes a list of k values as inputs and iteratively performs K-Means clustering for each of them. The average shadow width (\bar{x}_{sh}) is then taken according to equation (4). The uncertainty that was calculated for \bar{x}_{sh} is explained in section 2.3.

$$\bar{x}_{sh} = \frac{1}{N_i} \sum_{i=1}^{N_i} x_{sh,i}(k) \quad (4)$$

It was chosen as an acceptable range to use $k = 4, 5, 6, 7, 8$ clusters, and thus the number of iterations (N_i) equal to 5. This was because $k = 4$ allowed clusters for the pit shadow and other pit features to be segmented and $k = 8$ was the upper limit before the shadow cluster would become segmented into separate clusters itself. It was also an acceptable number of iterations before analysing a single image became too computationally intensive.

While this iterative clustering method solved the issues of quantifying the uncertainty in measurements of x_{sh} , the problem of how to measure the shadow width still remained. As the Sun can illuminate a planetary surface from a range of angles, where the shadow width should be measured will change between pits, or even between the same pit under different lighting conditions. Rather fortuitously, the sub-solar azimuth angle (ϕ) is given in the metadata files for HiRISE RDR images, which are made available through the Planetary Data System (PDS) Geosciences Node (<https://pds-geosciences.wustl.edu/>). This angle, ϕ , is the clockwise angle measured from a reference point to the sub-solar point. The sub-solar point is the location on the surface where the Sun is at zenith to an observer. In the case of MRO HiRISE images, figure 3 shows how the reference point is due-east such that the azimuth angle of due-north is 270° .

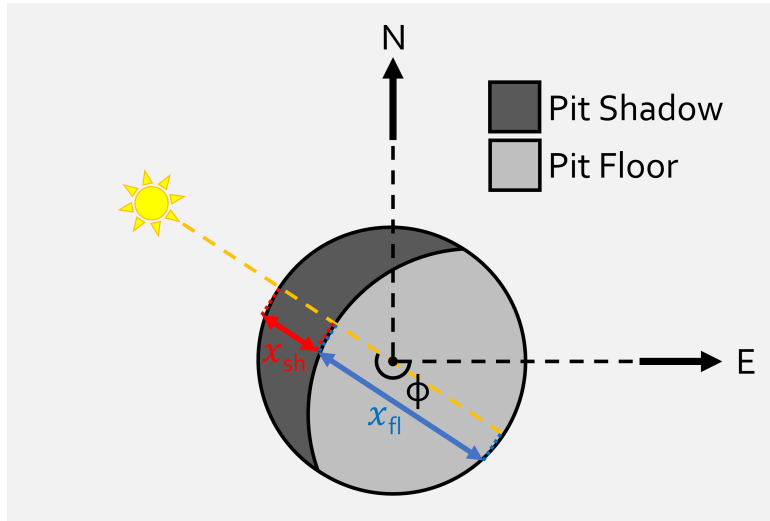


Figure 3: Schematic of how the shadow width is measured for an idealised pit as seen from orbit. ϕ in this diagram represents the sub-solar azimuth angle, which for HiRISE images is measured from east to the sub-solar point. The sub-solar point in this figure is directly below the cartoon Sun.

This information is used to rotate the binary shadow masks, which are produced during each iteration of K-Means clustering, such that the Sun is now incident from the top of the image and that the shadow is effectively horizontally aligned. Therefore, by finding the middle x coordinate of the shadow mask (not including background), MAPS is able to simply count downwards the number of pixels that were covered by shadow. Multiplying this pixel count by the resolution (in m/pixel) of the image then returns the shadow width (in metres).

A consequence of using an iterative approach is that it poses the question of whether the shadow mask should be saved as a shapefile for all values of k , or just one. Instead of randomly selecting a value for k , the binary shadow masks are actually summed together for all k values. Since a shadow pixel is given the value 1, and non-shadow a 0, then this effectively produces an array of pixel values, which contain how many times this pixel was extracted as a shadow. This array of pixel values is vectorised and saved as a shapefile layer with the same geo-reference as the input image, as shown in figure 4, with the number of detections as an attribute field. Pixels which have equal number of detections are also merged into the same feature to allow for easy selection and filtering. It should be noted that a given pixels number of detections is not the same as a measure of its confidence, since the shadow masks are not validated by any ground truth, here. However, it is the case that the more times a pixel was classified as a shadow throughout the iterative clustering, then the more likely it is a part of the pit's shadow.

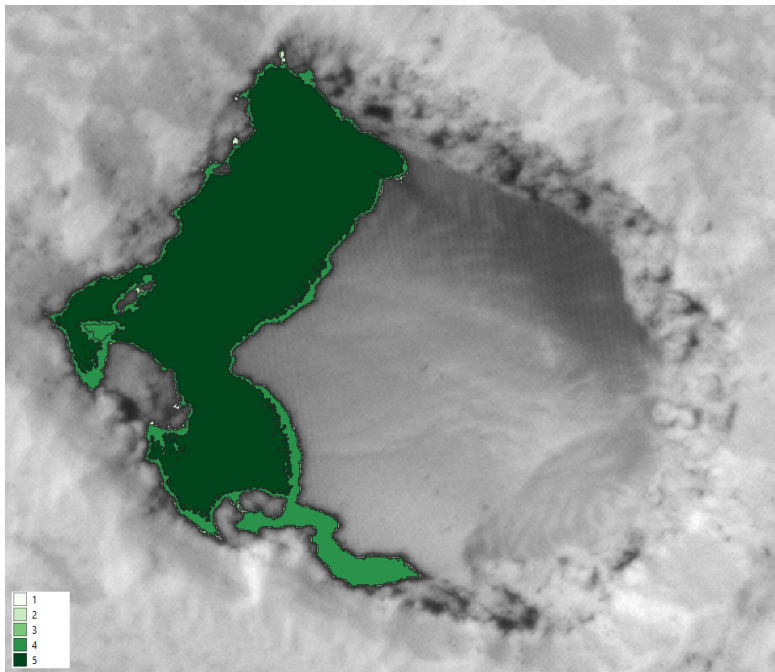


Figure 4: Screenshot of the shadow shapefile created using the method described in section 2.1 on the MGC³ feature APC130. This is the result of performing K-Means for values of $k = 4, 5, 6, 7$ and 8 on the HiRISE image ESP_052638_2020. This figure shows the features with shades of green according to the number of detections, with white being 1 and the darkest green being 5. (NASA/JPL/University of Arizona)

2.2 Apparent Depth Calculation

As mentioned previously, the MAPS tool uses equation (1) to determine the apparent depths (h) of Martian pits. Similarly to the sub-solar azimuth angle, the solar incidence angle (α) is also commonly given in the metadata files for images of planetary surfaces. However, h is not calculated after every iteration of K-Means clustering, rather equation (1) is applied to the average shadow width (\bar{x}_{sh}). The average shadow widths and apparent depths for each pit image, along with their uncertainties, are printed in the command line.

However, MAPS deliberately does not calculate the slope angle, nor the true depth, as was performed in [1]. In fact, MAPS does not assume all pits to be conical, as this was only a requirement to be able to estimate pit volumes, which MAPS does not do. It also means that $x_{sh} \geq D/2$ must always be true, otherwise the Sun will shine on the whole pit and there will be no shadow. Some examples of real Martian pits are shown in section 2.4, which suggest that this assumption is not always true.

Figures 5b and 5c show instances where the shadow will not project beyond the centre of the pit, compared to figure 5a which shows an example where the true depth could be calculated. In these

scenarios where $x_{sh} < D/2$, attempting to calculate the slope angle and true depth at $D/2$ using equations (2) and (3) would lead to a calculated value for H which is always smaller than h . It is for these reasons that it was deemed unnecessary for MAPS to calculate H .

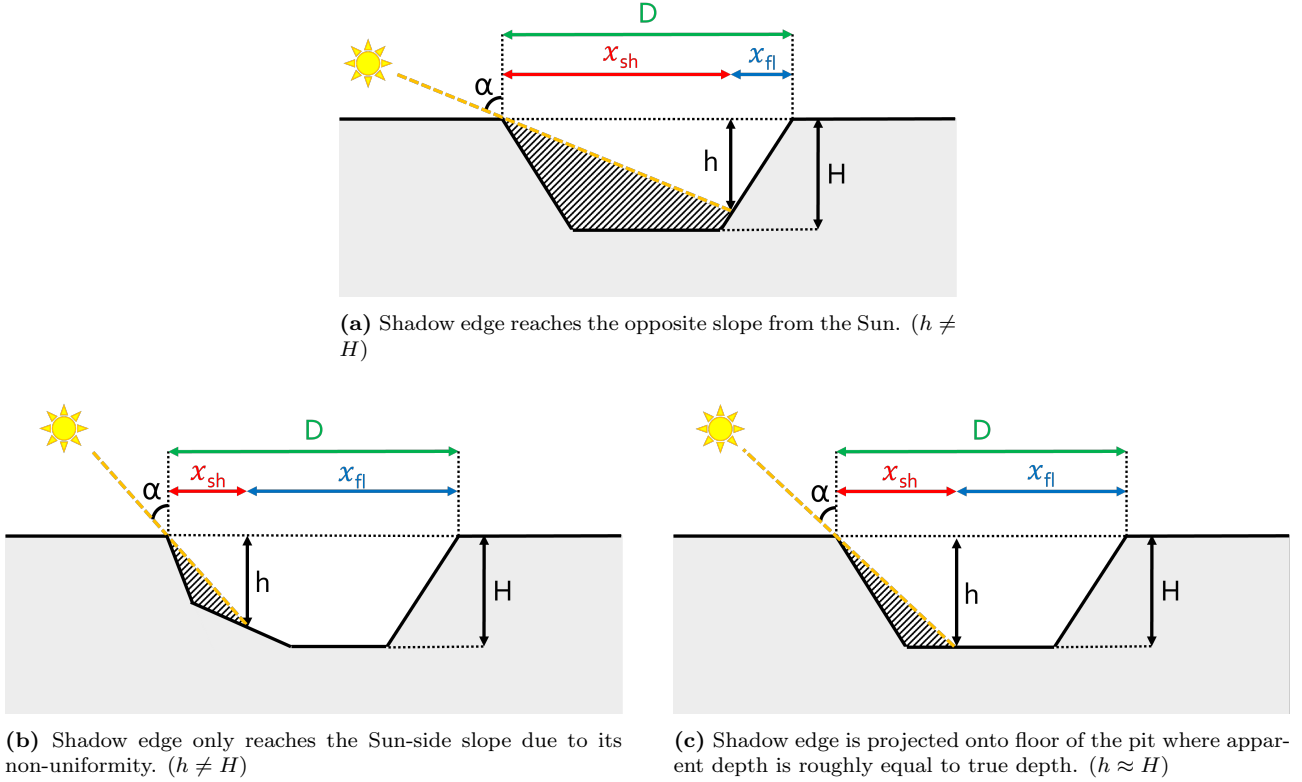


Figure 5: Examples of pits which under different lighting conditions will measure the apparent depth at different places, complicating the calculation of H . Scenario (a) would allow for the calculation of the opposite slope angle and thus H . In situations (b) and (c), H is not calculable as the slope is not uniform and the shadow reaches the pit floor, respectively.

2.3 Error Analysis

As MAPS has been designed to align the shadow mask and measure its width at the centre by counting the pixels, it is plausible to assume that the uncertainty would be a product of the sensor's resolution. In the case of the HiRISE camera on-board the MRO, this would mean that the uncertainty in the shadow width is $\approx \pm 0.25$ m. However, this is not the case for two reasons.

The first is that the number of clusters that the K-Means algorithm is tasked with segmenting the image into (k) tends to produce varying sizes of shadow mask. As k gets larger, the algorithm has more clusters to find in the same image. This means that the shadow mask appears to be eroded slightly, which has an impact on the measurement of its width. This was the motivation for using an iterative approach to K-Means clustering of pit images, since it allows the shadow width to be measured at a range of k values. As mentioned previously in section 2.1, an average is taken of these values is taken according to equation (4). The uncertainty in this average shadow width is calculated by taking the standard deviation of the shadow widths measurements at every k value. However, since MAPS does not place a threshold on how large the shadow must be in order to be extracted, this uncertainty may be very small for exceedingly thin shadows. As such, the largest uncertainty out of the standard deviation in shadow widths or the resolution of the image is assigned to each average shadow width measurements. For the MGC³ features described in section 2.4, in only one image out of six was the uncertainty due to varying k values smaller than the image resolution.

Secondly, there is also an uncertainty when rotating the shadow mask. As an image is made of

a grid of pixels, an image rotated by a angle which is not a multiple of 90° cannot fit back into this same grid perfectly, as shown by figure 6. When rotating typical RGB or grey-scale images, their pixel values are often interpolated to give the best representation of the image at this new orientation. However, as figure 6d displays, this would result in a shadow mask which contains pixel values that range from 0 to 1, rather than just ones or zeroes. This was not suitable for MAPS as for it to be able to count the pixels, they need to be definitively classified as a shadow or not. Therefore, the shadow masks were not rotated using interpolation, meaning that some shadow pixels may have changed location relative to others, thus affecting the shadow width measurements. This is difficult to quantify as no uncertainty has been given for the sub-solar azimuth angle, which is what the shadow masks are rotated by. Had it been, then rotation could have been performed for both the upper and lower bound of ϕ and an average taken. Although, this uncertainty should be on the same order as the pixel resolution as mentioned previously, since the shadow could be under any connected pixels.

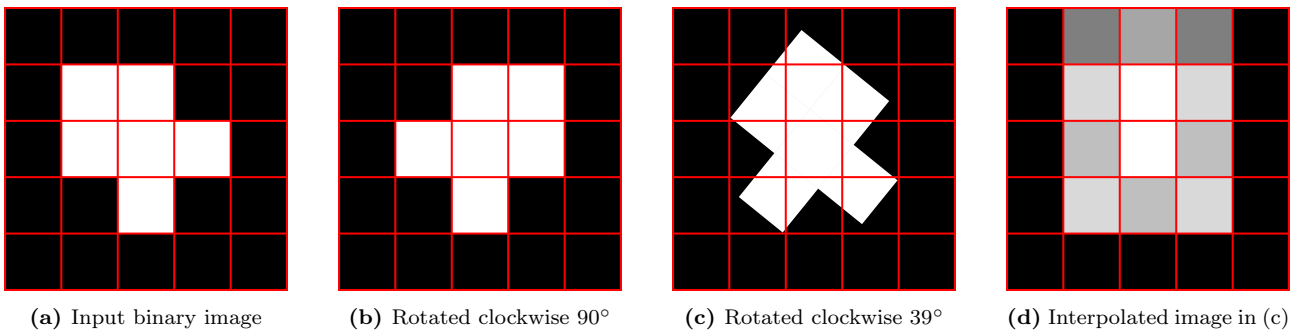


Figure 6: Diagram showing what happens when rotating a binary image by an angle that is not a multiple of 90° . (a) and (b) show the input binary image before rotation and the result of rotating it clockwise by 90° , respectively. Rotating this image around the centre pixel by 39° in (c) shows how the shape no longer perfectly fits within the grid of pixels. (d) shows a possible result of interpolating the rotated image, which produces a range of pixel values between 0 and 1.

Since there is no uncertainty provided for α for HiRISE images, the uncertainty in the apparent depth (σ_h) is calculated via error propagation and is given by equation (5).

$$\sigma_h = \sqrt{\left(\frac{\partial h}{\partial \bar{x}_{sh}}\right)^2 \sigma_{\bar{x}_{sh}}^2} = \sigma_{\bar{x}_{sh}} \tan(90^\circ - \alpha) \quad (5)$$

It is also expected that the process of how the input image is cropped to the extents of the pit will cause some variation in the calculated apparent depths. This is because using a label which contains more pixels will cause the K-Means algorithm to have more data points to cluster than previously. This would have the most pronounce effect on low values of k as this risks non-shadow pixels being included in the shadow mask. If the input image is more tightly cropped, then using higher values of k could lead to over-segmentation as there are fewer pixels to cluster. This has been purposefully not quantified due to the manner in which MAPS is intended to be used. MAPS is designed to be used after an object detection machine learning model (or other automated processes) has been classified to detect pits from HiRISE imagery. Each individual detection's bounding box is then used by MAPS as the label to crop the input image by. Therefore, any uncertainty in where the image is cropped to the extents of the pit is already accounted for by the accuracy/confidence score of the model's detection.

2.4 Initial Testing for Comparison with Elevation Data

For the purpose of this report, and to be able to prove the functionality of MAPS, the tool was applied to some examples of Martian pits. It was also necessary to retrieve some examples which had elevation data so that it could be confirmed that the calculated apparent depths are on the same order of magnitude. One of the largest databases for pit craters exists in the Mars Global Cave Candidate Catalog (MGC³) [15]. MGC³ is a catalogue of potential cave entrances on Mars, of which collapse pits are a candidate, with a large concentration present in the volcanic Tharsis region.

However, while this provided several features for testing, there was no guarantee that there would be any corresponding HiRISE imagery. Luckily, MGC³ is presented as point locations within an XML file (found at https://astrogeology.usgs.gov/search/map/Mars/MarsCaveCatalog/mars_cave_catalog). The catalogue could then be converted into an ESRI Shapefile layer by using the Java Mission-planning and Analysis for Remote Sensing (JMARS) GIS software [16]. This was necessary to be able to compare these feature locations with the footprints of all the HiRISE red-band imagery and derived Digital Terrain Models (DTMs). These DTMs are produced by considering the difference between two stereo HiRISE images of the same location, in order to calculate the elevation [17]. Using the QGIS ‘Extract by Location’ vector selection tool on these MGC³ and HiRISE footprint shapefiles, it was found which HiRISE imager and DTM products “contain” a MGC³ feature. This returned five MGC³ features, but unfortunately, two of these five were not suitable for testing as one was a potential cave entrance in the side of a cliff-face (CC0737) and the other is a natural bridge over a long linear depression (CC0870). This left the three features: APC130, CC0089 and CC0253 ((a), (b) and (c) in figure 7, respectively).

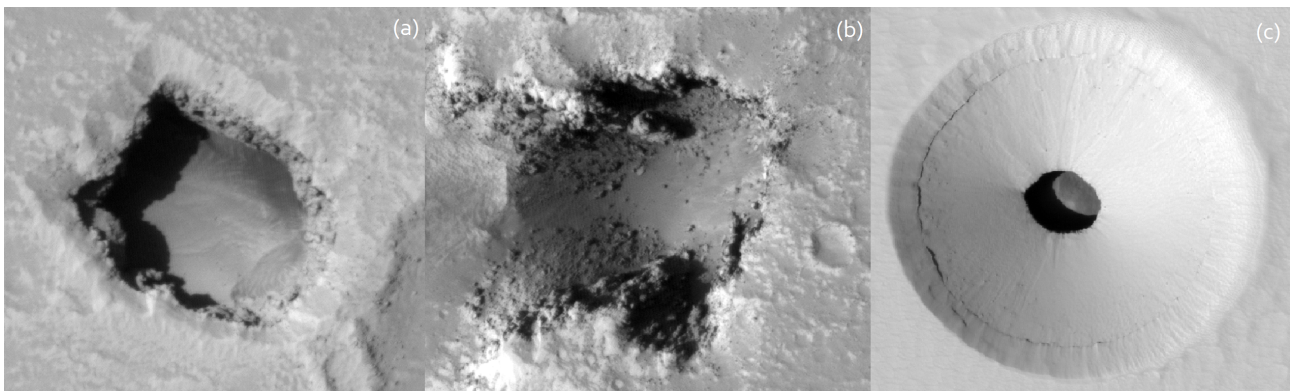


Figure 7: MGC³ features used for initial testing of the MAPS tool. (a) is described in MGC³ as a “collapse pit kinda like a APC [atypical pit crater]”; (b) is a “collapse floor of collapse pit”; and (c) is a “famous pit-floor cave on Pavonis” [15]. (a), (b) and (c) are all shown here in not-to-scale red-band HiRISE images, with product codes ESP_052638_2020, ESP_055209_2015 and ESP_023531_1840, respectively. (NASA/JPL/University of Arizona)

The reason for why this particular DTM was chosen was due to the need for a reference point when calculating the depth. As the apparent depth (h) is the depth of the pit at the edge of the shadow, this is where the depth should be retrieved from the DTM. However, whenever HiRISE images and corresponding DTMs of the same region of Mars’ surface are loaded into GIS software, it is noticeable that the features on the surface are not in the same places between the products. This is because the MRO satellite is in a different place in its orbit when the two images are taken. Therefore, a pixel coordinate which corresponds to the shadow edge in a HiRISE image, may relate to a completely different location on the surface in another image or in the DTM.

In order to work around this issue, the shadow was extracted, using the exact same method as in section 2.1, from the orthographic images which come as supplementary products to the HiRISE-derived DTMs. Orthographic images (or ortho-images) are stereo red-band HiRISE image pairs which have been rectified for effects due to topology [17]. As a result, ortho-images and DTMs of the same patch of surface will show features in exactly the same places. However, a consequence of orthorectifying images is that knowledge about the position of the satellite and Sun relative to the surface is lost. This means that, since a sub-solar azimuth angle no longer exists, the shadow masks extracted from ortho-images were instead rotated by their orientations, according to the scikit image regionprops function (see <https://scikit-image.org/docs/dev/api/skimage.measure.html#skimage.measure.regionprops> for more details).

Therefore, after this alignment, the initial and final coordinates of where the shadow width would normally have been measured (according to section 2.1) were found for each ortho-image. These

coordinates represent where the shadow meets the rim of the pit and where the shadow extends to within the pit. By finding the difference in elevation at these coordinates, the apparent depth (h) according to the HiRISE DTM was successfully measured. This method of finding h in the DTMs is also subject to the uncertainty of how the shadow mask can change under varying numbers of K-Means clusters. As such, the DTM depth was also measured iteratively over the same values of k for the HiRISE RDR images of the same three MGC³ features. Hence, an average of all DTM apparent depths was taken, with the uncertainty in this average being equal to the standard deviation of the DTM apparent depths for each value of k .

2.5 Testing on 88 Atypical Pit Craters

Once it had been confirmed to be performing as expected, the MAPS tool could then be tested on more features without the need for elevation data. The MGC³ was used here also, as the same shapefile used before was filtered down to only the atypical pit craters (APCs) which had corresponding HiRISE imagery. Using the QGIS same vector selection tool as in section 2.4 returned a total of 120 HiRISE red-band products whose footprints contained 98 separate APCs. This meant that there would be instances where multiple images were available for the same features, which allowed for more comparison of the effect of emission angles on variation in h . These 120 images were then downloaded from the Mars Orbital Data Explorer of the PDS Geosciences Node and manually labelled for every appropriate APC of these 98 features.

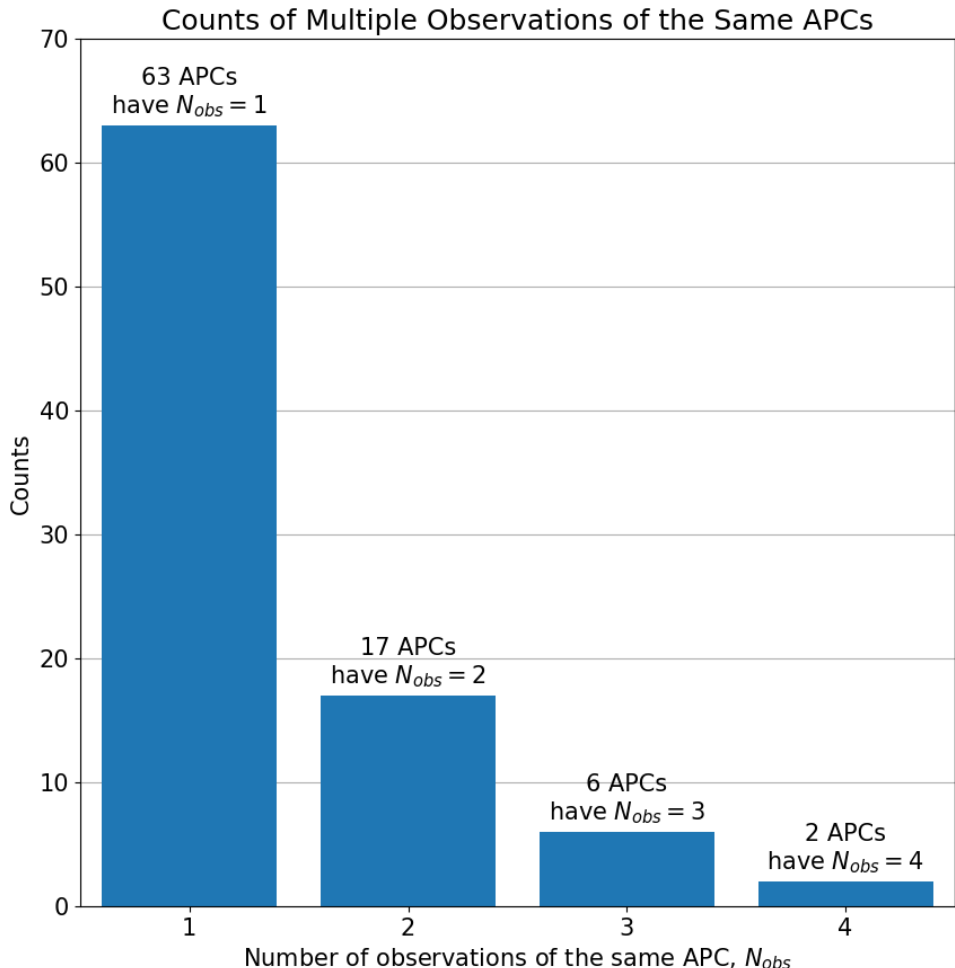


Figure 8: Instances where MGC³ APC features have been imaged more than once by HiRISE. 63 APCs have only got one corresponding HiRISE image, whereas 25 APCs have been imaged at least twice. Multiplying the counts for each bar by the corresponding N_{obs} and adding them altogether will reveal the total number of images, 123. The counts of multiple observations (where $N_{obs} > 1$) is expected to rapidly decrease if images are filtered to only very low emission angles.

APCs were labelled only if the full feature was included in the image; the pit did not show multiple similarly sized shadows; and if the feature was clearly a pit. Once labelling was completed, only 88 APCs remained, as on several occasions the above conditions were not met. As shown in figure 8, 25 of these 88 APCs have been observed more than once, meaning that 123 observations were available in total. These individual 123 images of Martian APCs were then passed through the MAPS tool, and the results of this are discussed below in section 3.2.

3 Results and Discussion

3.1 Results of Initial Testing

As displayed in table 1, applying the MAPS tool to the three MGC³ shown in figure 7 has successfully produced results for their apparent depths. The HiRISE DTM apparent depths also confirm that the shadow extraction employed by MAPS leads to apparent depth values on the correct order of magnitude. In terms of the apparent depths calculated by MAPS, table 1 shows that there is significant variation between different images in the cases of APC130 and CC0253. It was expected that since their morphologies are far more regular than that of CC0089, that h would be more consistent.

MGC ³ Code	HiRISE Product ID	h [m]	DTM h [m]	ϵ [deg]	α [deg]
APC130	ESP_052638_2020	36.0 ± 1.7	37.4 ± 2.4	8.3	41.3
	ESP_060379_2020	15.3 ± 0.3	22.9 ± 0.8	29.0	40.1
CC0089	ESP_055209_2015	31.4 ± 4.0	13.7 ± 1.1	22.9	50.9
	ESP_060260_2015	24.5 ± 1.6	15.3 ± 1.1	10.6	36.5
CC0253	ESP_023531_1840	23.8 ± 0.8	23.4 ± 0.7	4.1	34.4
	ESP_023953_1840	12.1 ± 0.5	19.5 ± 0.5	20.8	35.4

Table 1: Comparisons between calculated apparent depth values and HiRISE DTM data for three MGC³ features. Here, h is the apparent depth, ϵ is the emission angle of the Mars Reconnaissance Orbiter, and α is the solar incidence angle. All values have been rounded to one decimal place, as to not claim a precision of several decimal places, while also to avoid rounding down uncertainties to zero had no decimal places been given.

In order to explain this unexpected result, the sensing conditions and the average shadow width measurements of the pits were investigated. Large variation is also seen in the average shadow width measurements for APC130 and CC0253. This would be an expected result had the solar incidence angles (α) been sufficiently different to allow for such range in shadow sizes. However, as table 1 shows, α only ranges on the order of $\approx 1^\circ$ for APC130 and CC0253, implying that α is not responsible for the variation in h . Another factor that can change the width of the observed shadow is the emission angle (ϵ) of the HiRISE camera. ϵ is the angle between the satellite and a normal drawn from the surface, essentially the satellite analogue of α . With a larger ϵ , the shadow cast by the Sun into the pit will appear smaller to the spacecraft than if it were to be looking straight down. Table 1 shows that this was true for APC130 and CC0253, as h was smaller when ϵ was greater. This resulted in an apparently thinner shadow, despite a relatively constant α .

The same trend is not displayed for CC0089, although in this case α between its two HiRISE images are not similar. This resulted in different lighting conditions and meaning that ϵ cannot solely be attributed to any variation. In fact, for CC0089 the angles ϵ and α appear to counteract each other as a higher α casts a greater shadow while a lower ϵ means the satellite will observe the shadow to be slimmer, and vice versa. While it would appear from these features that large ϵ values can lead to inaccurate, or variation in, calculated apparent depth values, six images of three features are not enough data points to draw a confident conclusion. Nonetheless, the emission angle for cannot be corrected for within the scope of MAPS, as the spacecraft azimuth angle is not given in the same way it had been for the Sun for HiRISE images. While the phase angle between the spacecraft and the Sun is given, whether it is a clockwise or anticlockwise angle is not known. Therefore, it may be necessary to put an upper limit on the value of ϵ that an image can have for the pit depth to be calculated.

With regards to comparing these h values to the apparent depths calculated from the HiRISE DTMs, there is an important caveat that needs to be addressed. This particular DTM dataset is not created by any sort of radar or laser altimetry, but are instead calculated via photoclinometry [17] - the process of estimating depth in 2D images on the same scene based on how the light and shading changes. Therefore, the DTM apparent depths in table 1 should not be treated as ground truth as the dataset was produced using a similar concept to the calculation of h in MAPS. As mentioned previously, calculating the apparent depths from these HiRISE-derived DTMs was only to ensure the calculated values for h were on the correct order of magnitude. There is also the concern that the ortho-images, which were used to find the correct reference points to calculate the depths from, also show shadows of different size and shape, despite being ortho-rectified. Consequently, there is also some variation in the DTM depths for different images of the same pits.

3.2 Results of Testing on 88 Atypical Pit Craters

As is annotated in figure 9, the MAPS tool calculated a minimum and maximum apparent depth (h) of 10.9 and 221.3 m, respectively, in the 123 observations of 88 atypical pit craters. It was also found that the most abundant range in h was between 25 and 50 m. Interestingly, this finding does not agree with the depth values that are given for each APC as part of the MGC³ database. However, it is not clear in the literature how these depths were derived. Thus they cannot validate each h value calculated by MAPS, but it is appropriate to compare them as sample sets on a more macroscopic scale. Depths found in the ranges 50 to 75 m and 75 to 100 m are the joint-most abundant in the MGC³, as shown by figure 9. In addition, this was determined after having corrected the MGC³ catalogue for repeat observations of the same APCs, meaning that this discrepancy is not due to a different total count.

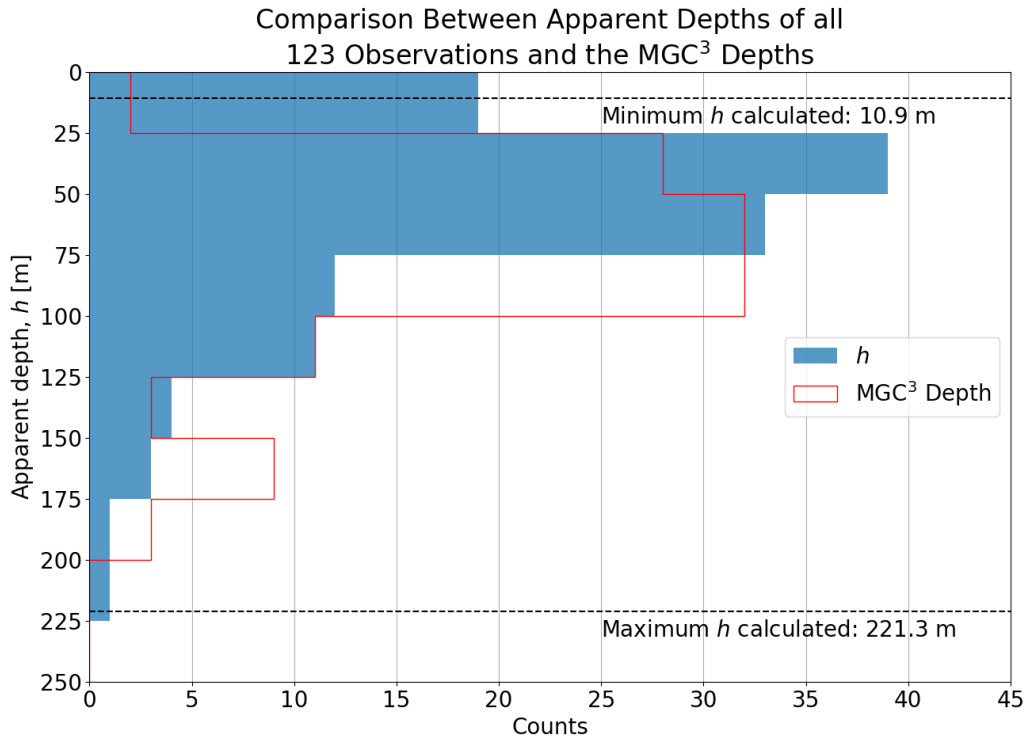


Figure 9: Histogram of the apparent depths that were calculated by MAPS for all 123 observations. The red outline represents the depths for each APC as provided by the MGC³, although it is not clear of their source. Both the h and MGC³ depth profiles include the instances where pits have been imaged more than once by HiRISE.

Instead, this is likely a result of scenarios where some pits at these sub-100 m apparent depths exhibit the largest relative uncertainties (σ_h/h), as displayed by figure 10. With larger relative uncertainties at smaller h values, it will be increasingly likely that a value could fall into neighbouring depth ranges. There are three instances where the relative uncertainty exceeds 20%, which have been investigated to find the cause (the HiRISE product IDs are given in brackets): APC092

(ESP_019997_1975_RED_2), APC137 (ESP_057764_1775_RED_1) and APC140 (ESP_063829_1755_RED). In this particular image of APC137, a very thin shadow is present. A dimly-lit sloping rim has also been incorrectly included in the shadow mask for one iteration of K-Means. Whereas, APC092 and APC140 are cases where $\epsilon > 20^\circ$ and there are several dimly-lit features that have been mis-classified as shadows for some but not all iterations of K-Means. These three results imply that the values of k that are used for K-Means clustering in MAPS, as well as the average pixel value threshold for what clusters are classified as shadows, requires calibration. Figure 10 also suggests that there is no correlation between the size (in diameter and in depth) of the pit and the relative uncertainty in the calculated apparent depth. This means that MAPS can be confidently applied to pits with a range of sizes without the concern that a larger or even smaller pit will lead to larger uncertainties.

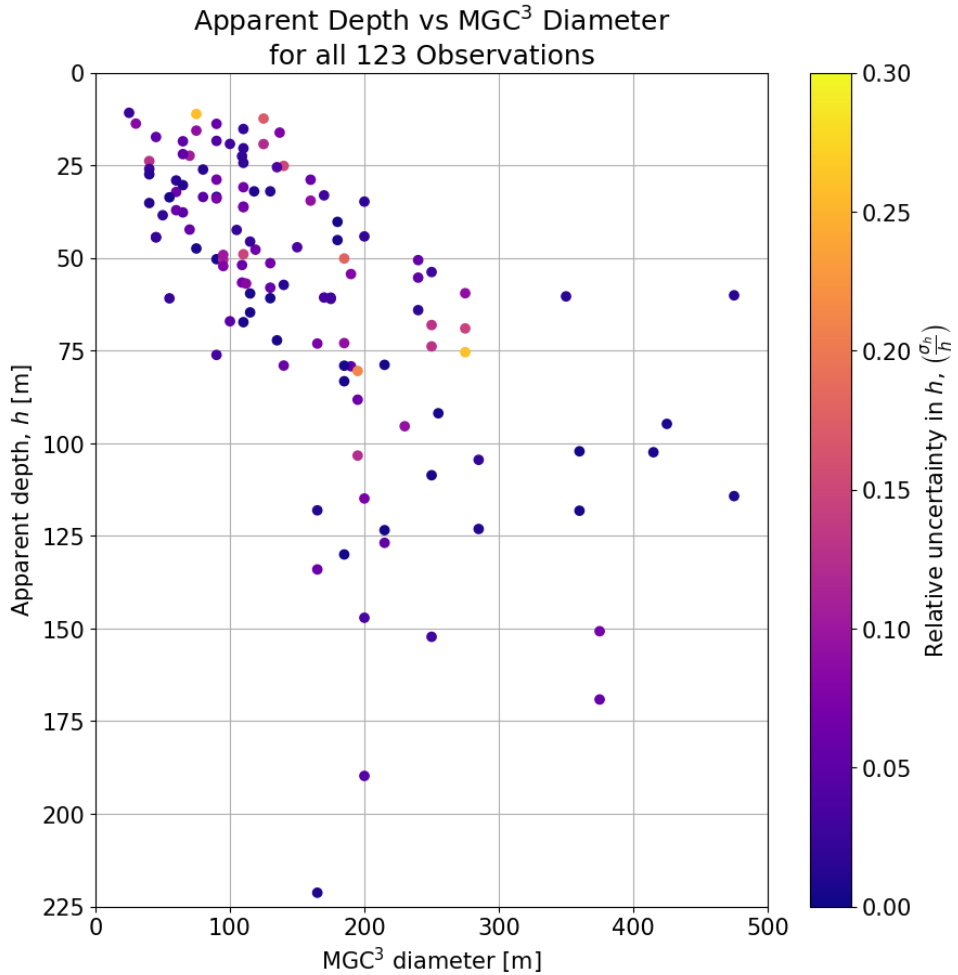


Figure 10: Apparent depth calculations for all 123 observations against the APC's diameter according to MGC³. The colour bar to the right of the figure shows the relative uncertainty (σ_h/h) of each observation. This shows that the size of the pit has no correlation with the relative uncertainty in h , meaning that no feature size limit is necessary with MAPS.

However, the main purpose of this next testing phase was to further investigate the role that the emission angle of the HiRISE camera relative to surface may play in varying the calculated apparent depth. Figure 11 shows that there is general trend that beyond $\Delta\epsilon \approx 15^\circ$ one can expect to see calculated h values for the same pit which vary by more than 50%. APC130 and APC054 have been singled out in figure 11 as examples of extreme variation in h (222.4% and 150.9%, respectively). This variation is not caused by any irregularity in their shapes, but rather by at least one of their multiple corresponding images having an emission angle larger than 20° . The reason why the solar incidence angles were plotted also, is to show that these factors are all intertwined. It may appear that the differences in α may also cause variation in h , but this is only because of the large emission angles. Had the emission angles all been very low or near-zero, then it would be expected that this same plot of $\Delta\alpha$ would be far more precisely grouped and show far less percentage difference in h . This is the

case as α is a factor in calculating h , whereas ϵ cannot be corrected for. The only way in which large ϵ values could be accounted for within the scope of MAPS is by implementing a limit to the maximum ϵ values that an image can have to be fed through the tool.

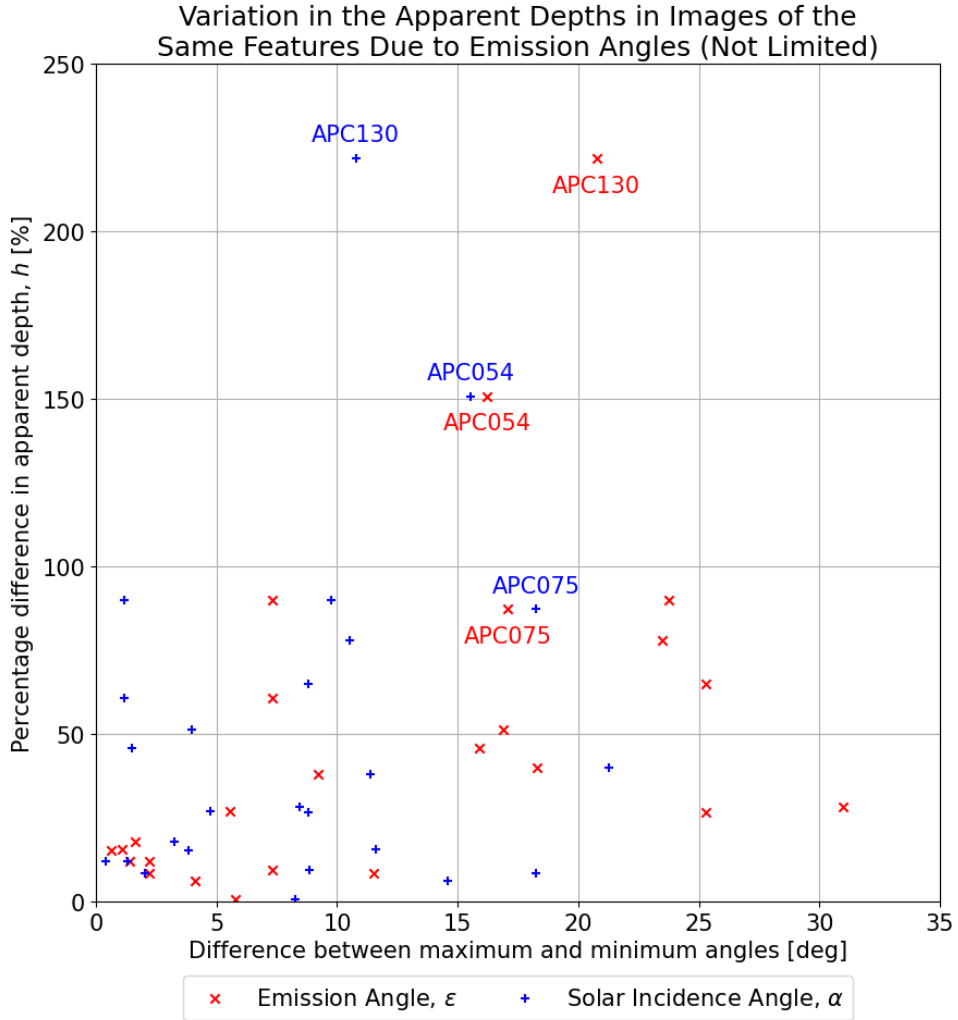


Figure 11: Variation in the apparent depth calculations for APCs that have been imaged more than once by HiRISE. The red data points represent the difference between the maximum and minimum emission angles for multiple images of the same pit. Whereas the blue are the same, but for the solar incidence angles. APC130 and APC054 show very large variation, while APC075 has been pointed out for reference with figures 12a and 12b.

Figure 12 shows that by filtering out the results from images with large emission angles greatly reduces the percentage difference in h values in cases of multiple observations of the same feature. The same is also true for the solar incidence angle, which confirms that the main cause of variation is h is due to large emission angles. Figures 12a and 12b display the percentage differences in h for each pit when all emission angles larger than 20° and 10° are excluded. $\epsilon < 20^\circ$ and $\epsilon < 10^\circ$ were only arbitrarily chosen here to demonstrate the point. For such a limit to be correctly implemented into MAPS, calibration would need to be performed in order to find the ϵ limit which yields the lowest percentage difference, while also not losing data about too many features. Limiting the 25 pits which had repeat observations to $\epsilon < 20^\circ$, reduced this number to only 20. Doing the same for $\epsilon < 10^\circ$ left only 15 features. Therefore, MAPS needs to be applied to larger sets of features with more repeat observations to be able to calibrate to find this balance.

The percentage differences in h of the images which cover APC075 have been identified in figures 12a and 12b as it is an example of significant variation in h despite large emission angles having been filtered out. Three images cover APC075, each with emission angles of 0.6° , 7.5° and 17.7° , respectively. While the results for the image with $\epsilon = 17.7^\circ$ are not removed for figure 12a, it was expected

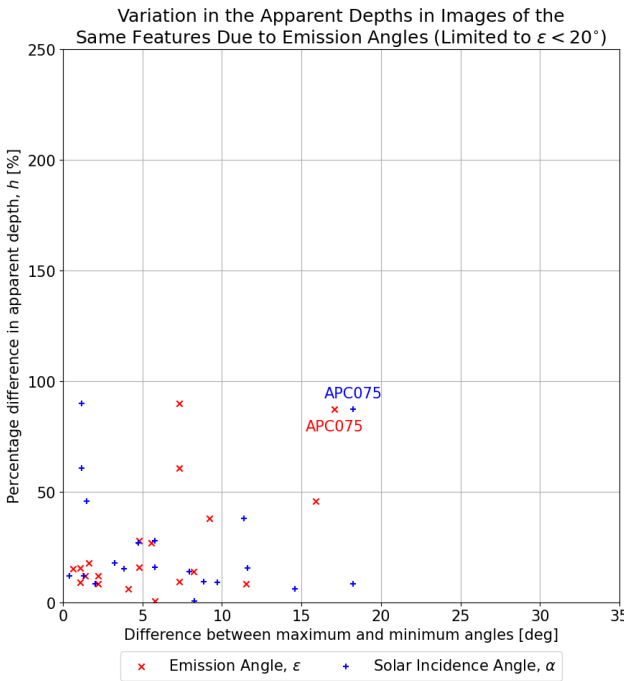
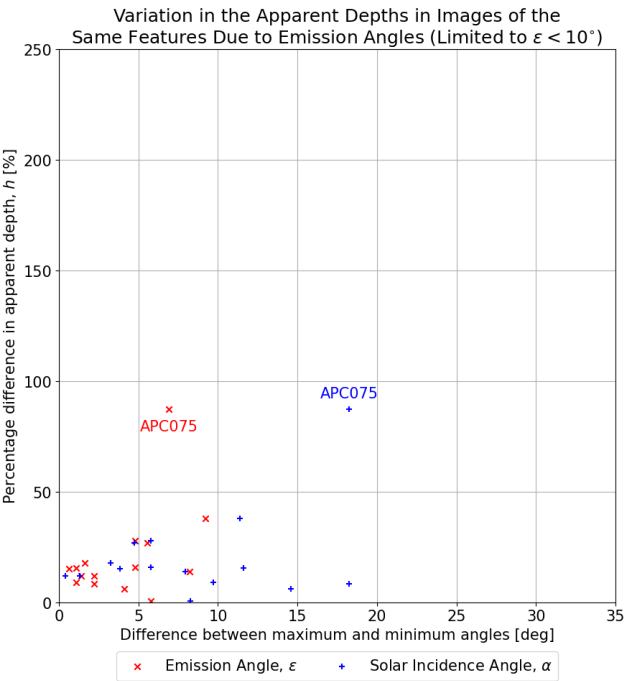
(a) $\epsilon < 20^\circ$ (b) $\epsilon < 10^\circ$

Figure 12: Variation in the apparent depth calculations for APCs that have been imaged more than once by HiRISE, but limited to what emission angles the images can have. (a) shows the variation in h on the same axis scale as in figure 11 for $\epsilon < 20^\circ$. (b) shows the same but for $\epsilon < 10^\circ$.

that the percentage difference in h would decrease after it was filtered out in figure 12b. As figure 12b shows, this was not true since the images with the lower emission angles actually exhibit the minimum and maximum h values for APC075. The images displayed in figure 13 show APC075 to be a very circular pit showing no signs of irregularity, which in two of the three images is completely covered in shadow.

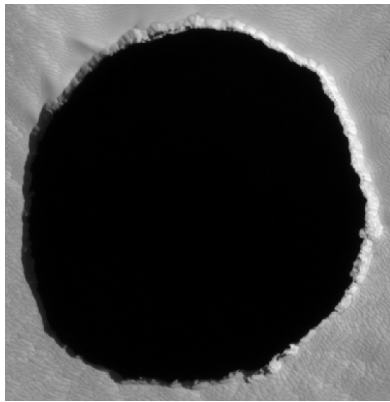
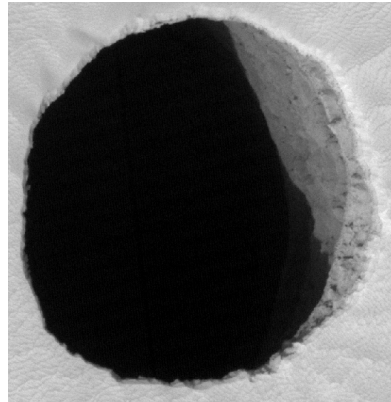
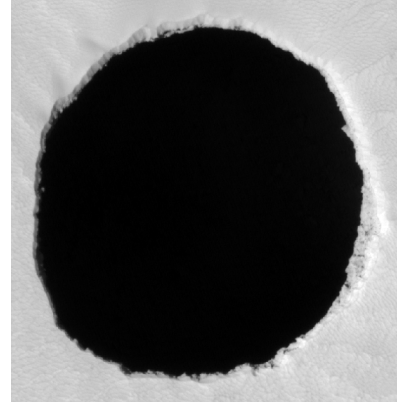
(a) $\epsilon = 0.6^\circ, \alpha = 52.3^\circ$ (b) $\epsilon = 17.7^\circ, \alpha = 41.2^\circ$ (c) $\epsilon = 7.5^\circ, \alpha = 34.1^\circ$

Figure 13: Images of the MGC³ feature APC075 which the MAPS tool was tested upon. (a) and (c) show that the feature remains completely covered in shadow despite a change in the Sun's location in the sky, while (c) shows the HiRISE camera is able to see the inner walls of the pit due to a large emission angle. The HiRISE product IDs displayed here are (from left to right) PSP_003647_1745_RED, PSP_004847_1745_RED, and PSP_005770_1745_RED, (NASA/JPL/University of Arizona)

Interestingly, the image where the full feature is not blanketed by shadow is the image with the largest emission angle. However, the solar incidence angle varies from 34.1 to 52.3° between the two images which show full shadow coverage. As the emission angles for these two images are relatively low, this means that the average shadow width that is measured did not significantly change, in spite of a difference in the Sun's position. What can be deduced from this is that APC075 is sufficiently deep

that it will remain covered in shadow for all solar azimuth angles (as it is circular) if $\alpha > \tan(\bar{x}_{sh}/H_{sh})$, where H_{sh} is the true depth of the pit at the edge of the shadow. Therefore, the apparent depths calculated by MAPS for pits whose interiors are completely covered in shadow should be treated with caution, as it is unlikely that $h = H_{sh}$ in these scenarios.

4 Limitations and Future Improvement

While the MAPS tool has improved upon previous work to automate the process of shadow extraction and apparent depth calculation from Martian pits, it comes with some limitations on how it can be used. For example, MAPS is only designed to be used on images which are cropped to the extents of a pit. MAPS is not, however, designed to extract or detect shadows in large images with many surface features in them. MAPS should also only be used on regular pits, although the tool will still run successfully when applied to pits with irregular morphologies. This particularly extends to pits which exhibit multiple similarly sized shadows, because it was found that at different values of k the K-Means method extracted two completely separate shadows in CC0089.

Unlike previous studies of pit morphologies [1], the MAPS tool does not any assume or give any indication on the shape of the pit, only its apparent depth (h). It was also considered during development to measure \bar{x}_{sh} and calculate h at every pixel along the shadow's edge rather than just at the centre. It was thought that this could give an indication of the profile of the pit's floor. However, it was noticed that the shadows for regularly-shaped pits taper off towards the ends. This means that the calculation for h at each pixel would in the majority of cases become increasingly smaller the further they were from the centre, resulting in constant predictions of concave pit floors. Future work could involve analysing the similarity in the shapes of the pit rims and shadows, since a perfectly flat pit floor would show a shadow with an identical shape to the rim that cast it.

There still remain several input parameters that require calibration in order to improve the precision of the shadow extraction, as well as to reduce the variation in h for images of the same features. These parameters are listed as follows:

- The average pixel value threshold for a K-Means cluster to be classified as a shadow cluster (currently set to 30).
- The range of numbers of clusters which the K-Means algorithm has to segment the image into (currently $k = 4, 5, 6, 7$ and 8).
- The upper limit to what emission angle an image is allowed to have in order for MAPS to be applied to it (limits of 10 and 20° have been experimented with so far).
- Minimum area that the shadow mask must meet in order to be classified as a shadow (not currently in use).

The current values for each parameter was chosen based on how the tool performed during testing. Therefore, these parameters will likely require calibration before being applied to new datasets of Martian pits (or pits on other bodies). The first parameter, the average pixel value threshold, may be calibrated by considering the difference between the pixel values of the shadows and the surrounding background. With sufficient knowledge of what pixel values do not correspond with a shadow, a less arbitrary threshold could be found. For the range of k values and the emission angle limit, it may be necessary to create artificial images of Martian pits as a means of calibration. For example, with the necessary ‘fake’ elevation data and defining a position for the Sun in the sky, the pixels that would theoretically be covered in shadow could be found. Additional noise could be applied to the rest of the image to simulate surrounding terrain. With large amounts of these fake images and DTMs, the values for both parameters could be found that minimise both the data lost through limiting ϵ , but also the variation in h .

The method of shadow extraction and apparent depth calculation described in this report would also be highly applicable to data taken by other sensors, or data taken of other terrestrial planetary bodies. The only way in which MAPS is specific to HiRISE imagery in its current state is in the way that it reads the corresponding image metadata files which contain the necessary sensing information. It would not take significant effort for the MAPS tool to be broadened in this aspect.

5 Conclusion

This report has presented the MAPS (Martian Pit Shadow Extractor) tool and how it can successfully extract the shadow from a single-band HiRISE image of a Martian pit and calculate the pit depth. MAPS employs an iterative K-Means clustering process to segment the image into clusters such that the darkest one(s) (the shadow) can be selected. This iteration also means that MAPS can produce geo-referenced shadow shapefile layers with separate features for how many times each pixel was extracted as a shadow. This allows the user to filter out the features such that only the most detected pixels remain. With the assistance of sensing information available for HiRISE images, the width of the shadow masks produced via K-Means are measured such that the apparent depth of the pit can be calculated by MAPS.

During the development of MAPS, the methods described in this report were tested on three examples of Martian pits from the Mars Global Cave Candidate Catalog (MGC³). It was found for two of the three features that there was significant variation in the measured average shadow widths between images of the same feature, despite the fact that there was no significant change in solar incidence angle (α), nor sub-solar azimuth angle (ϕ). It was expected that if the Sun had not changed position in the sky relative to the surface, that the size of the shadow should remain the same. However, for the same two features, their two stereo images were taken at noticeably different emission angles (ϵ). Therefore, ϵ is most likely responsible for this variation.

Ultimately, three features was too small of a sample set to confidently draw any conclusions. As a result, MAPS was tested on more examples of Martian pits - 123 images of 88 MGC³ APCs to be exact. Of these features, 25 of them had multiple corresponding HiRISE images. This allowed for a comparison between the difference between the minimum and maximum emission angles and the percentage difference in h values for images of the same feature. This unveiled significant variation in h in scenarios where the emission angle changes dramatically, up to 222.4% in one case. Limiting the results to only those images with an emission angle less than 20°, and furthermore 10°, progressively reduced the percentage differences observed in h . During this testing phase, it was also found that there exists no correlation between the size of the pit, in either diameter or apparent depth, and the relative uncertainty in h . This means that there should be no concerns over whether MAPS is limited to what scale of features it can accurately extract the shadow from.

The most instrumental application of MAPS would be as a post-processing step in a machine learning object detection pipeline which has been trained to detect Martian pits. The shadow shapefiles could potentially be used as another source of training labels to specifically detect pits that project shadows onto their interiors. Notwithstanding the naming of the tool, the plan for the future is to adapt MAPS such that it can read in the necessary sensing information from other sources. Ideally, MAPS could soon be applied to analyse pits found in data from other satellites in orbit around Mars, but also other planetary bodies where pits are present.

References

- [1] Danielle Wyrick, David A. Ferrill, Alan P. Morris, Shannon L. Colton, and Darrell W. Sims. Distribution, morphology, and origins of martian pit crater chains. *Journal of Geophysical Research: Planets*, 109(E6), 2004.

- [2] David A. Ferrill. *Pit*, pages 1–6. Springer New York, New York, NY, 2021.
- [3] William R. Halliday. "Pit Craters", lava tubes, and open vertical volcanic conduits in Hawaii: a problem in terminology. *International Journal of Speleology*, 27:113–124, 1998.
- [4] David A. Ferrill, Danielle Y. Wyrick, and Kevin J. Smart. Coseismic, dilational-fault and extension-fracture related pit chain formation in Iceland: Analog for pit chains on Mars. *Lithosphere*, 3(2):133–142, 04 2011.
- [5] Gerald A. Galgana. *Caldera*, pages 1–15. Springer New York, New York, NY, 2021.
- [6] Peter J. Mouginis-Mark and Scott K. Rowland. The geomorphology of planetary calderas. *Geomorphology*, 37(3):201–223, 2001.
- [7] D. Y. Wyrick, D. L. Buczkowski, L. F. Bleamaster, and G. C. Collins. Pit Crater Chains Across the Solar System. In *41st Annual Lunar and Planetary Science Conference*, Lunar and Planetary Science Conference, page 1413, March 2010.
- [8] Carolyn H. van der Bogert, James W. Ashley, and David Ferrill. *Pit Crater*, pages 1–7. Springer New York, New York, NY, 2014.
- [9] Péter Gadányi and Carolyn H. van der Bogert. *Lava Tube*, pages 1–7. Springer New York, New York, NY, 2014.
- [10] Francesco Sauro, Riccardo Pozzobon, Matteo Massironi, Pierluigi De Berardinis, Tommaso Santagata, and Jo De Waele. Lava tubes on earth, moon and mars: A review on their size and morphology revealed by comparative planetology. *Earth-Science Reviews*, 209:103288, 2020.
- [11] K.E. Williams, Christopher P. McKay, O.B. Toon, and James W. Head. Do ice caves exist on mars? *Icarus*, 209(2):358–368, 2010.
- [12] M.S. Robinson, J.W. Ashley, A.K. Boyd, R.V. Wagner, E.J. Speyerer, B. Ray Hawke, H. Hiesinger, and C.H. van der Bogert. Confirmation of sublunarean voids and thin layering in mare deposits. *Planetary and Space Science*, 69(1):18–27, 2012.
- [13] Adnan Ahmad. Deep learning driven detection of Martian pits. *ACRI-ST Internship Report*, 2021.
- [14] G. Nodjoumi, R. Pozzobon, and A. P. Rossi. Deep Learning Object Detection for Mapping Cave Candidates on Mars: Building Up the Mars Global Cave Candidate Catalog (MGC³). In *52nd Lunar and Planetary Science Conference*, Lunar and Planetary Science Conference, page 1316, March 2021.
- [15] G. E Cushing. Mars Global Cave Candidate Catalog PDS4 Archive Bundle. *PDS Cartography and Imaging Sciences Node (IMG)*, 2015.
- [16] P. R. Christensen, E. Engle, S. Anwar, S. Dickenschied, D. Noss, N. Gorelick, and M. Weiss-Malik. JMARS - A Planetary GIS. In *AGU Fall Meeting Abstracts*, volume 2009, pages IN22A–06, December 2009.
- [17] R. L. Kirk, E. Howington-Kraus, M. R. Rosiek, J. A. Anderson, B. A. Archinal, K. J. Becker, D. A. Cook, D. M. Galuszka, P. E. Geissler, T. M. Hare, I. M. Holmberg, L. P. Keszthelyi, B. L. Redding, W. A. Delamere, D. Gallagher, J. D. Chapel, E. M. Eliason, R. King, and A. S. McEwen. Ultrahigh resolution topographic mapping of mars with mro hirise stereo images: Meter-scale slopes of candidate phoenix landing sites. *Journal of Geophysical Research: Planets*, 113(E3), 2008.

6 Appendix

MGC3 ID	HiRISE DTM ID	HiRISE Product IDs	Used for testing?
APC130	DTEEC_052638_2020_060379_2020_A01	ESP_052638_2020 ESP_060379_2020	Yes
CC0089	DTEEC_055209_2015_060260_2015_A01	ESP_055209_2015 ESP_060260_2015	Yes
CC0253	DTEEC_023531_1840_023953_1840_A01	ESP_023531_1840 ESP_023953_1840	Yes
CC0737	DTEEC_014327_1675_013971_1675_A01	ESP_013971_1675 ESP_014327_1675	No
CC0870	DTEEC_069174_2045_001420_2045_A01	PSP_001420_2045 ESP_069174_2045	No

Table 2: MGC³ features which were found to have available HiRISE RDR Version 1.1 imagery and derived DTM data. This figure gives the product codes of the HiRISE images that cover the features and the DTMs that were produced from them, as well as whether they were used for initial testing.

MGC ³ Code	HiRISE Product ID	h [m]	σ_h [m]	σ_h/h	ϵ [deg]	α [deg]
APC001	ESP_057434_1790_RED_1	10.9	0.3	0.02	2.5	43.3
APC005	PSP_009488_1745_RED_1	13.8	1.1	0.08	3.8	58.6
APC006	ESP_058700_1785_RED	26.0	0.7	0.03	5.7	31.8
APC007	ESP_058489_1785_RED	23.9	3.0	0.13	5.7	31.9
APC008	ESP_057988_1735_RED	35.2	0.4	0.01	3.1	34.0
APC009	ESP_066876_1785_RED	27.5	0.4	0.01	2.3	42.9
APC011	ESP_066599_1755_RED	17.4	0.9	0.05	4.2	43.7
APC012	ESP_059702_1790_RED_1	44.5	1.1	0.02	1.3	36.3
APC013	ESP_059702_1790_RED_2	44.4	1.0	0.02	1.3	36.3
APC014	ESP_065887_1660_RED	38.5	0.8	0.02	5.4	48.1
APC015	ESP_066942_1735_RED	15.7	1.4	0.09	0.5	40.4
APC016	PSP_009989_1760_RED	33.7	0.2	0.01	0.4	57.9
APC017	ESP_059557_1740_RED	60.9	1.4	0.02	0.1	36.0
APC022	ESP_058133_1770_RED	22.0	1.1	0.05	7.5	34.0
APC023	PSP_007774_1745_RED	37.1	2.2	0.06	6.8	50.2
	PSP_008130_1745_RED	32.2	2.0	0.06	6.2	54.1
APC025	ESP_067707_1840_RED	29.1	0.4	0.01	9.5	41.5
APC027	ESP_058687_1810_RED	37.7	1.8	0.05	0.2	32.2
APC029	ESP_046753_1610_RED	18.5	0.9	0.05	0.2	53.6
APC030	PSP_009488_1745_RED_2	30.4	0.4	0.01	3.8	58.6
APC032	ESP_057645_1770_RED	22.4	2.4	0.11	0.8	40.1
APC033	ESP_057434_1790_RED_2	42.4	2.4	0.06	2.5	43.3
APC034	ESP_016622_1660_RED	47.5	0.3	0.01	0.1	55.4
APC038	ESP_058845_1780_RED	33.6	1.6	0.05	0.5	31.2
APC039	ESP_057750_1870_RED	26.2	0.3	0.01	3.7	44.9
APC040	ESP_055614_1605_RED	18.4	0.8	0.04	3.6	54.7
APC041	ESP_057777_1790_RED	33.5	0.5	0.01	1.9	39.3

Table 3: Results from testing MAPS on 88 MGC³ atypical pit craters (APCs). In cases where a HiRISE image contains more than one feature, the product idea is appended with an integer from 1 to how ever many features are present. The images themselves are identical, but the separate names were necessary when using the labels for each feature to clip the images.

MGC ³ Code	HiRISE Product ID	<i>h</i> [m]	σ_h [m]	σ_h/h	ϵ [deg]	α [deg]
APC042	ESP_013167_1785_RED	76.2	2.5	0.03	8.2	49.4
	ESP_013589_1785_RED	50.4	0.4	0.01	25.0	45.5
APC043	ESP_058199_1785_RED	34.0	2.4	0.07	7.9	34.1
	ESP_063434_1780_RED	50.5	6.0	0.12	5.2	55.6
APC045	ESP_066929_1780_RED	52.2	4.0	0.08	1.3	42.0
	PSP_009765_1780_RED	49.2	5.0	0.10	5.4	56.5
APC048	ESP_057025_1640_RED	24.4	0.4	0.02	3.9	42.0
APC049	ESP_056946_1665_RED	42.5	0.9	0.02	2.9	43.1
APC050	ESP_042085_1795_RED_1	67.4	0.4	0.01	6.7	39.4
APC052	ESP_031285_1785_RED	20.4	0.4	0.02	8.0	41.7
APC054	ESP_033935_1805_RED	51.9	3.2	0.06	8.4	45.0
	ESP_036770_1805_RED	56.7	3.7	0.07	9.5	54.7
	ESP_041900_1805_RED	22.6	0.4	0.02	24.6	39.2
APC055	ESP_061772_2020_RED	56.9	4.8	0.08	5.8	42.3
APC056	ESP_038076_1795_RED	59.6	0.4	0.01	8.9	57.7
	ESP_042085_1795_RED_2	64.7	0.3	0.00	6.7	39.4
APC059	ESP_057830_1820_RED	32.1	0.3	0.01	1.2	40.6
APC061	ESP_028450_1730_RED	47.8	3.1	0.06	0.0	55.9
APC062	ESP_058542_1625_RED	58.1	3.4	0.06	0.2	30.2
APC065	ESP_066863_1660_RED	12.4	2.1	0.17	6.8	38.3
	PSP_005203_1730_RED_1	60.9	0.3	0.01	5.5	35.6
APC068	PSP_005625_1730_RED_1	32.1	0.4	0.01	12.8	34.5
APC071	ESP_033342_1660_RED	79.1	4.7	0.06	0.4	44.0
	ESP_050089_1660_RED	57.3	0.7	0.01	9.7	32.6
APC072	PSP_005058_1720_RED	60.7	2.0	0.03	6.2	37.3
	ESP_036454_1660_RED	45.2	0.3	0.01	6.9	62.1
APC074	ESP_053781_1660_RED	40.3	0.2	0.00	8.3	60.8
	PSP_003647_1745_RED	118.1	1.4	0.01	0.6	52.3
APC075	PSP_004847_1745_RED	134.1	7.9	0.06	17.7	41.2
	PSP_005770_1745_RED	221.3	1.8	0.01	7.5	34.1
APC076	ESP_057975_1810_RED	73.1	5.2	0.07	5.3	37.9
	ESP_028793_1655_RED	50.2	9.0	0.18	0.1	57.1

MGC ³ Code	HiRISE Product ID	<i>h</i> [m]	σ_h [m]	$\sigma_{h/h}$	ϵ [deg]	α [deg]
APC079	ESP_011677_1655_RED	61.1	2.2	0.04	9.5	58.2
	ESP_012600_1655_RED	60.7	1.7	0.03	3.7	49.9
APC082	ESP_049812_1735_RED	130.0	0.6	0.00	24.9	29.1
	ESP_050234_1735_RED	79.1	0.4	0.01	2.2	31.6
APC084	PSP_004913_1735_RED	73.0	6.7	0.09	9.7	39.6
	PSP_005836_1735_RED	83.3	0.4	0.01	1.4	33.4
APC085	ESP_019351_1795_RED	79.3	4.2	0.05	3.2	54.7
	ESP_019984_1795_RED	54.4	4.3	0.08	19.1	56.2
APC086	ESP_019997_1975_RED_1	189.8	8.1	0.04	29.1	52.5
	ESP_029043_1975_RED_1	147.1	5.3	0.04	8.6	55.5
APC089	PSP_003317_1975_RED_1	114.9	8.3	0.07	3.8	61.3
	PSP_005203_1730_RED_2	126.9	6.6	0.05	5.5	35.6
APC090	PSP_005625_1730_RED_2	78.9	0.4	0.00	12.8	34.5
	ESP_030995_1610_RED	64.1	1.0	0.02	3.3	37.7
APC091	ESP_056867_1695_RED	53.8	1.5	0.03	5.5	44.7
	ESP_011756_1735_RED	152.2	4.7	0.03	22.2	55.6
APC092	PSP_005414_1735_RED	108.7	0.6	0.01	3.9	34.3
	ESP_019997_1975_RED_2	75.5	19.6	0.26	29.1	52.5
APC093	ESP_029043_1975_RED_2	69.0	10.1	0.15	8.6	55.5
	PSP_003317_1975_RED_2	59.5	5.4	0.09	3.8	61.3
APC094	PSP_006693_1755_RED	123.2	1.3	0.01	8.4	38.1
	PSP_006904_1755_RED	104.5	2.3	0.02	6.8	41.3
APC095	ESP_033618_2050_RED	60.4	0.8	0.01	5.0	38.6
	ESP_011386_2065_RED	150.7	10.1	0.07	6.7	61.0
APC096	ESP_011531_2065_RED	169.2	9.8	0.06	8.9	61.4
	ESP_016411_1605_RED	114.3	1.0	0.01	0.2	56.8
APC098	ESP_024481_1605_RED	60.1	0.7	0.01	23.9	47.1
	ESP_033355_1635_RED	47.1	1.7	0.04	6.6	45.8
APC099	ESP_021738_1625_RED	123.5	0.5	0.00	8.7	44.0
	ESP_045830_1735_RED	51.4	3.3	0.06	2.3	53.0
APC100	ESP_042128_2090_RED	91.9	0.4	0.00	2.0	41.3
	ESP_043974_2090_RED	28.9	1.7	0.06	7.0	39.4

MGC ³ Code	HiRISE Product ID	<i>h</i> [m]	σ_h [m]	$\sigma_{h/h}$	ϵ [deg]	α [deg]
APC108	ESP_042629_2090_RED	102.2	0.3	0.00	2.6	39.6
	ESP_063477_2090_RED	118.2	0.4	0.00	3.6	51.2
APC109	ESP_043763_2100_RED	55.3	2.8	0.05	11.4	38.8
	ESP_071022_2100_RED	50.6	2.8	0.05	4.1	47.6
APC110	ESP_042985_2100_RED	45.6	1.0	0.02	7.4	39.0
	ESP_053547_2095_RED	34.6	3.2	0.09	2.5	41.7
APC112	ESP_042932_2050_RED	67.1	3.4	0.05	5.8	39.0
	ESP_042721_2045_RED	13.8	0.8	0.06	1.2	39.2
APC114	ESP_043222_2035_RED	72.3	0.4	0.01	9.9	39.2
	ESP_014077_1660_RED	34.8	0.6	0.02	3.8	34.6
APC117	ESP_058186_1660_RED	44.2	0.9	0.02	9.4	29.9
	ESP_016978_1730_RED	73.9	9.6	0.13	1.5	54.3
APC119	ESP_017189_1730_RED	68.1	8.9	0.13	13.1	56.3
	ESP_017544_2055_RED	94.8	0.6	0.01	0.3	42.7
APC121	ESP_059544_1650_RED_1	16.2	1.2	0.07	0.1	39.4
	ESP_059544_1650_RED_2	19.3	2.3	0.12	0.1	39.4
APC125	ESP_025892_1780_RED	95.4	8.9	0.09	2.0	51.1
	ESP_052638_2020_RED	36.2	1.6	0.04	8.3	41.3
APC126	ESP_055196_2015_RED	49.0	7.2	0.15	22.3	50.9
	ESP_060379_2020_RED	15.2	0.3	0.02	29.0	40.1
APC129	ESP_062924_2020_RED	30.9	2.1	0.07	21.0	49.2
	ESP_041162_1665_RED	33.1	1.0	0.03	9.2	34.9
APC133	ESP_066005_2110_RED	25.2	3.8	0.15	4.1	71.1
	ESP_058898_1775_RED	19.3	0.5	0.03	1.8	31.3
APC134	ESP_057764_1775_RED_3	36.3	2.5	0.07	3.7	39.0
	ESP_057764_1775_RED_2	28.9	1.9	0.07	3.7	39.0
APC136	ESP_057764_1775_RED_1	11.2	2.9	0.26	3.7	39.0
	ESP_066507_1610_RED	25.5	1.0	0.04	1.0	40.1
APC137	ESP_044748_2110_RED	102.5	0.8	0.01	8.3	40.1
	ESP_051829_1755_RED	88.3	5.3	0.06	0.7	47.0
APC138	ESP_063262_1755_RED	103.4	12.7	0.12	31.7	54.5
	ESP_063829_1755_RED	80.5	17.0	0.21	21.7	55.5